Interfacial Reactivity and Speciation Emerging from Na-montmorillonite Interactions with Water and Formic Acid at 200°C: Insights from Reactive Molecular Dynamics Simulations, Infrared Spectroscopy, and X-ray Scattering Measurements

Murali Gopal Muraleedharan,[a*] Hassnain Asgar,[b*] Seung Ho Hahn,[a*] Nabankur Dasgupta,[c] Greeshma Gadikota,[b,†] Adri C.T. van Duin [a,†]

[a]Department of Mechanical Engineering, Pennsylvania State University, State College, PA

[b]School of Civil and Environmental Engineering, Cornell University, Ithaca, NY 14853

[c]Department of Engineering Science and Mechanics, Pennsylvania State University, State College, PA

[†]Corresponding authors

*Equal contribution

Abstract

Reactive organic fluid - mineral interactions at elevated temperatures contribute to the evolution of planetary matter. One of the less studied but important transformations in this regard involves the reactions of formic acid with naturally occurring clays such as sodium montmorillonite. To advance a mechanistic understanding of these interactions, we use ReaxFF reactive molecular dynamics simulations in conjunction with infrared (IR) spectroscopy and X-ray scattering experiments to investigate the speciation behavior of water-formic acid mixtures on sodium montmorillonite interfaces at 473 K and 1 atm. Using a newly developed reactive forcefield, we show that the experimental IR spectra of unreacted and reacted mixture can be accurately reproduced by ReaxFF/MD. We further benchmark the simulation predictions of sodium carbonate and bicarbonate formation in the clay interlayers using Small and Wide-Angle X-ray Scattering measurements. Subsequently, leveraging the benchmarked forcefield, we interrogate the pathway of speciation reactions with emphasis on carbonate, formate, and hydroxide groups elucidating the energetics, transition states, intermediates, and preferred products. We also delineate the differences in reactivities and catalytic effects of clay edges, facets, and interlayers owing to their local chemical environments, which have far reaching consequences in their speciation behavior.

The experimental and simulation approaches described in this study and the transferable forcefields can be applied translationally to advance the science of clay-fluid interactions for several applications including subsurface fluid storage and recovery and clay-pollutant dynamics.

Keywords: ReaxFF, Molecular Dynamics, IR spectroscopy, X-ray scattering, clay minerals, speciation, surface chemistry, reactive interfaces

1. Introduction

Advancing experimentally supported predictive insights into reactive phenomena at fluid-solid interfaces is essential for gaining scientific insights into the evolution of matter on planets. In this context, reactions involving montmorillonite clays in aqueous and formic acid environments is of particular interest. Montmorillonite clays are identified in different carbonaceous chondrites [1–3] that are pieces of asteroids that remained unprocessed on earth since the formation of our solar system.[4] These chondrites contain various forms of organic matter including aliphatic and aromatic hydrocarbons, carboxylic acids, and alcohols.[4] Moreover, the organic materials were also deposited in the early earth at metamorphic conditions with the weathering products of intermediate and mafic rocks, which are primarily montmorillonite clays.[1,5] Furthermore, formic acid is the simplest carboxylic acid and is often observed to be remaining or left over after the building of meteorites and comets.[6] Additional organic materials could be buried in Earth's subsurface through geologic and tectonic processes.[1] In this context, the aim of this study is to probe the reaction mechanisms involved in the interactions of sodium montmorillonite with formic acid and water at an elevated temperature of 200 ^{0}C, especially how the hierarchical 2D nanoscale structure of Na-montmorillonite [7] and the intercalation of Na^{+} ions contribute to differences in the chemical interactions at the basal plane, edge or facet of Na-montmorillonite.

Several complex and competing reactions occur as Na-montmorillonite reacts with aqueous formic acid environments. [8–10] Na-montmorillonite undergo surface hydroxylation and proton generation reactions in aqueous environments, which further triggers a chain of other reactions, such as the formation of hydroxides. [11–13] These reactions contribute to structural and morphological changes of clay solids. [14–16] Chemical interactions between organic acids and water with montmorillonites can result in the formation of carbonate species that eventually neutralize the dissolved cations and precipitate within the interlayers. [17,18] The formation of carbonates has been shown to change the interlayer spacing and the resulting swelling behavior in sodium montmorillonite. [17,18] Despite these observations, significant knowledge gaps remain in the interactions of Na-montmorillonite with water and formic acid at elevated temperatures. Uncertainties regarding the intermediates that are formed leading

to the observed phases, associated reaction energy barriers, and differences in the reactivity of the clay mineral facet, interlayers, and edge exist. To address these challenges, the following questions are addressed in this study:

1. What new phases and species are formed as Na-montmorillonite clay reacts with water and formic acid? How does reactivity influence the interlayer basal spacing of the clay structure?
2. What are the possible reaction pathways leading to the formation of observed phases?
3. How do the differences in the chemistry of the facet, interlayer, and edge of sodium montmorillonite influence reactivity?

To address these questions, computational models such as ReaxFF/MD and experimental approaches such as Fourier-Transform Infrared Spectroscopy (FT-IR) and X-ray scattering measurements are used to investigate reactivity and speciation when sodium montmorillonite reacts with formic acid and water. Although numerical simulation approaches such as Monte Carlo (MC) methods, [19–21] Molecular Dynamics (MD), [22–24] and Density Functional Theory (DFT) [25,26] have been used to study the interfacial dynamics of fluids in clays, ReaxFF/MD methodology [27,28] is uniquely suited to elucidate the interfacial chemical reaction mechanisms [29] and to estimate early-stage kinetics [16] in reactive fluid-solid systems. ReaxFF allows the user to set up an appropriate initial geometry and then harness the reaction-diffusion processes to drive the system towards local chemical equilibria. In contrast with a non-reactive MD simulation with non-reactive empirical potentials, where the system topology remains constant throughout the simulation, this feature of ReaxFF methodology makes it much more general. ReaxFF forcefields are trained against the dataset obtained from accurate electronic structural calculations such as density functional theory (DFT), which enables near-quantum mechanical accuracy, especially for reaction barriers and enthalpies, circumventing the high computational costs of ab-initio based methods. For these reasons, ReaxFF based MD simulations have been used to accurately simulate the dynamics of mineral/fluid interfacial chemistry in prior studies [15,16,29,30]. In this study, we probe the reactive interactions of Na-montmorillonite with formic acid and water using a hybrid simulation and experimental approach. In this study, we probe the reactive interactions of Na-montmorillonite with formic acid and water using a hybrid simulation and experimental approach. In this study, we probe the reactive interactions of Na-montmorillonite with formic acid and water

using a hybrid simulation and experimental approach. We further analyze the system to delineate reactivity of different types of interfaces within the system that are challenging to probe experimentally, like the difference in reactivity of a mineral edge, facet, and the interlayer regions when exposed to the same fluidic environments.

2. Materials and Methods

2.1 Experimental Methods and Materials

Na-montmorillonite (SWy-3) clay was obtained from The Source Clays Repositories (Purdue University, West Lafayette, IN) and used as received. Formic acid with purity in the range of 98-100% (EMSURE® ACS, Reag. Ph Eur) was purchased from Millipore Sigma. To determine the reaction products, ~500 mg of clay powder was reacted with 100% water and 1:1 mixture of formic acid and water at 200°C, 1 atm for 2 hours. The reactions were carried out in an acid digestion vessel (Parr Instrument Company). After the reactions, the powders were filtered to remove the liquids and air-dried at 90 °C for 48 hours. To evaluate changes in the chemical bonds as a result of reaction, the infrared (IR) spectra were acquired in an Attenuated Total Reflection (ATR) mode using an Attenuated Total Reflection-Fourier Transform Infrared spectrometer (ATR-FTIR, NicoletTM iS50, Waltham, MA). The spectrum of unreacted clay was also acquired as a control. The IR spectra were acquired in the range of 4000 – 500 cm^{-1} with the spectral resolution of 1 cm^{-1} and signal averaged over 32 scans. Additionally, to uncover the changes in various functional groups, spectra in specific range were also deconvoluted into Gaussian profiles using the OriginPro 2017 with the help of 'Multiple Peak Fit' analysis tool. The deconvolutions were performed in two different frequency ranges of 3800-2650 cm^{-1}, and 1800-1300 cm^{-1} since dominant changes to the spectra were observed in these regions. The R-squared (R^2) values corresponding to the coefficient of determination (COD) for each deconvolution fit were also reported. The R^2 value is the percentage of the response variable variation that explains the fitted regression line. A typical R^2 value is always between 0 and 1. If the value is 0, it indicates that the fitted line does not explain any variability of the response data around its mean. However, if R^2 is 1, it indicates that the fitted line explains all the variability of the response data around its mean.

In our fits, we noted an R^2 value of > 0.99 in all cases, which indicates a good fitness of fits and reliable agreement between the modeling fits and the experimental data.

To determine the changes in the microstructure and structure, multi-scale Ultra-Small, Small and Wide-Angle X-ray Scattering (USAXS/SAXS/WAXS) measurements were performed at Sector 9-ID-C at Advanced Photon Source (APS) in Argonne National Laboratory (ANL). The instrument at 9-ID-C uses the original Bonse-Hart double-crystal setup [31,32]. To obtain the scans, the powdered samples were sandwiched between a clear scotch tape and loaded on the acquisition plate. The scattering from the empty tape was also taken as background and subtracted from the data. The X-ray wavelength, energy and total flux during the measurements were 0.59 Å, 21.0 keV, and ~10^{13} photon mm^{-2} s^{-1}, respectively. Calibrations for sample-to-detector distance and instrument were performed using silver behenate for SAXS[33] and LaB_6 for WAXS. USAXS, SAXS, and WAXS data were obtained by reducing the collected data using the Irena[34] and Nika[35] macros in the IgorPro software (Wavemetrics, Lake Oswego, OR).

2.2 ReaxFF/reactive Molecular Dynamics Simulations

ReaxFF is a bond-order dependent potential, wherein the total energy of the system consists of contributions from bond-order dependent terms and nonbonded interaction terms. The ReaxFF bond order is calculated based on the interatomic distances of all atom pairs in every time step. Energy contributions from bond-order dependent terms such as bond, valence angle, and torsion angle disappear upon bond dissociation, and only the nonbonded interactions such as van der Waals and Coulombic energies need to be considered thereafter. The connectivity between all atom pairs is calculated on-the-fly from the local atomic environment and updated every time step of the simulation. This feature allows ReaxFF to capture the chemical reaction process systematically. Atomic charges required to calculate the non-bonded interaction energies is a dynamic quantity and derived using the electronegativity equalization method (EEM) [36]. More details on the ReaxFF functional form and implementation can be found in references [21] and [47] .

To model atomic interactions in Na-montmorillonite, we started with the Na/Si/O/H ReaxFF parameterization from Hahn *et al.* [38] and combined it with the Si/Al/O/H ReaxFF parameters which were previously reported by Pitman and van Duin [30] for clay-zeolite composites. We then augmented the training set with the sodium carbonate (Na_2CO_3) and bicarbonate ($NaHCO_3$) groups as well as the vibrational normal modes of carbonate ion to ensure accurate reproduction of the IR spectra (ref: Supplementary Material, Section 1). Although the Pitman and van Duin parameter set were extensively tested to study the structure of Ca-montmorillonite within the zeolite housing and cation/water diffusion under conditions of dynamic chemical equilibrium, a well-trained Na-related parameter set is critical for describing the hydration of the Na-montmorillonite surfaces and the subsequent leaching processes. The Na/Si/O/H parameters used in this study were trained against a DFT-based training set which describes, sodium-water binding energies, hydration of sodium hydroxide with water and sodium ion interactions with silanol (Si-OH). All the given training dataset are relevant to the chemical dissolution of silica/silicate/silicalite surfaces in the presence of sodium cations and therefore, could provide a reliable description of sodium leaching dynamics, chemisorption and physisorption of water molecules at the Na-montmorillonite surface. Furthermore, the parameterization of the Pitman and van Duin model along with its extensions had been tested for different crystalline and amorphous structures.[39–43] This has also captured the enhanced sodium ion diffusion behavior in water at elevated temperatures due to the disruption of hydrogen bonds of water in solvation shell.[44,45] The Na/Si/Al/O/H parameter set employed herein are suitable for studying the structure and dynamics of sodium transport under varying temperature and solvation conditions.

Na-montmorillonite is a dioctahedral phyllosilicate with a 2:1 arrangement of tetrahedral silicate and octahedral aluminum layers. The crystalline Na-montmorillonite structure used for the simulations consisted of 11200 atoms created using a unit cell with lattice parameters a = 5.22 Å, b = 9.02 Å, and c = 12.4 Å. This structure was first independently energy minimized with the (001) cleavage plane exposed to vacuum and leveraged the reactive forcefield for surface atomic rearrangements and optimization. Following this, the system is equilibrated at T = 298 K and P = 1 atm with periodic boundary conditions but leaving 2 Å of vacuum on either side of the free surface. The space between the TOT (tetrahedral-octahedral-tetrahedral) layers contain sodium cations (Na^+).

The overall structure of Na-montmorillonite has a negative charge which is balanced by the positively charged intercalated Na^+ ions.

Single water and formic acid molecules were independently created and allowed to relax to the lowest energy configuration within the force field. We chose 13600 fluid molecules each for both water and formic acid and were randomly arranged around the Na-montmorillonite structure on all sides of the system until the desired density was achieved corresponding to the chosen temperature (T = 473 K) and pressure (P = 1 atm). Thereafter, the energy of the system was minimized and non-reactively equilibrated at target temperature and pressure, to form a system geometry (**Figure 1**), thereby exposing crystal facet, edge, and the interlayers to fluid molecules to create avenues for protonation and other surface reactions.

We used ReaxFF integrated into the Amsterdam Density Functional (ADF) [46] for reactive MD simulations. All simulations were run in the anisotropic isothermal-isobaric (NPT) ensemble with fixed x and y dimensions, using a weak Berendsen thermo/barostat with a temperature damping constant of 0.1 ps to keep the temperature constant. A time step size of 0.25 fs was used, and the equations of motion were integrated using the velocity-Verlet integration scheme [47]. The system was run for 0.6 ns allowing for the generation of sufficient statistics. A total of three independent repetitions of the simulation starting from different initial geometries were performed; their mean values were obtained to ensure an unbiased statistical sampling of the MD trajectory. We also used ReaxFF/MD implementation in LAMMPS [48,49] to generate the data necessary for computing IR spectra. For this, the system was run in NPT ensemble for a maximum of 20 ps. For the IR spectra calculation, the output in the form of the total dipole moment of the system was obtained every 0.5 fs, which was later post-processed to compute the IR spectra [50].

3. Results and Discussion

3.1 Speciation behavior

The first step is to benchmark the reactive forcefield by ensuring that the different species signatures observed in ATR-IR spectra are accurately predicted by the simulation. **Figure 2 (a)** and **2 (b)** represent the measured and

computed IR spectra respectively. As can be seen from these figures, roughly, three frequency regimes can be identified characteristic of different types of vibrational modes: 3800-2650 cm^{-1}, 1800-1300 cm^{-1}, and 1300-500 cm^{-1}. These regimes were also deconvoluted into Gaussian peaks to classify them based on representative species, as shown in **Figures S10 and S11**.

In **Figure 2 (a)**, the IR peak around ~515 cm^{-1} is associated with the bending vibrations of Si-O-Al of pristine Na-montmorillonite crystal [51]. Upon reacting with both the fluids, a slight shift to a higher wavenumber i.e. from 516.70 cm^{-1} (unreacted) to 516.74 cm^{-1} (after reactions), was also noted for the Si-O-Al linkages. Importantly, heights of these peaks were influenced by the chemistry of surrounding fluids: reactivity with H_2O yielded the largest decrease in height followed by the 1:1 mixture of H_2O and HCOOH and HCOOH. Computed IR peaks also showed similar characteristics for the Si-O-Al linkages. In **Figure 2 (b)**, the computed IR peak corresponding to the bending vibrations of Si-O-Al linkages in unreacted Na-montmorillonite crystal is observed around ~430 cm^{-1}. This peak decreases in height upon reaction with various fluids and also shifts marginally to higher wavenumber (~440 cm^{-1}), similar to the experimental IR data. Note that there is ~86 cm^{-1} difference between the experimental and computed frequencies, because the forcefield was not directly fitted to the Si-O-Al vibrational frequencies. Additionally, computed IR peaks corresponding to pure HCOOH shows the largest reduction in peak height contrary to the experiments, suggesting that the simulations have overpredicted the reactivity of HCOOH with Na-montmorillonite surface. To further investigate the physical reasons behind peak intensity shifts, we calculated the angle distribution of Si-O-Si (**Figure S5(a)**) and Si-O-Al (**Figure S5(b)**) before and after the reactions. It is evident from **Figure S5** that there is a broadening of these angles after reaction, which could be attributed to the peak shifts to higher frequencies. This observation is further validated by prior studies reporting the broadening of angles due to the formation of surface silanol (Si-OH) groups [15,16].

Corroborating evidences were also observed from the peaks associated with the hydroxyl groups, where it is interesting to note that no shifts were observed in the bending vibrations of hydroxyl groups (δ OH) of Al-Al-OH (~914.7 cm^{-1}) and tridymite (~796 cm^{-1}) in Na- montmorillonite. This observation also directed our attention to investigate changes in silanol (Si-OH) groups. The IR bands around ~1115 cm^{-1} and ~1000 cm^{-1} which are

typically attributed to the Si-O (out-of-plane) and Si-O (in-plane) stretching vibrations, respectively [51–53] were determined for Na-montmorillonite samples. However, a reduced intensity of IR spectra that corresponds to Si-O bonds when Na-montmorillonite is reacted in water is observed, which may be attributed to the bond dissociation of Si-O-Si followed by silanol formation. We also observed a shift from 982.81 to 1000.78 cm^{-1} for Si-O in-plane stretching vibrations as a result of the reactions. However, for the ReaxFF/MD case, the frequencies were slightly underpredicted (red-shift) for the Si-O (in-plane) case which is located at ~800 cm^{-1} whereas for the Si-O (out-of-plane) case, the predictions fall in place of ~1100 cm^{-1}. Nonetheless the general trend of reduction in intensity post-reaction remained unchanged.

Furthermore, as seen in the deconvoluted peaks in **Figures S10**, in the unreacted clay, the prominent bending vibrations were observed at 1647.54 cm^{-1} and 1632.94 cm^{-1}. These peaks correspond to -OH bending vibrations. In the reacted Na-montmorillonite, similar vibrations were observed but the peaks were slightly shifted. For example, in Na-montmorillonite reacted with water, the aforementioned peaks were observed at 1626.77, 1581.65, 1544.31, and 1366.57 cm^{-1}, respectively. In addition to a slight shift in the peak positions, the peak around 1581.65 cm^{-1} became prominent and appeared as a shoulder peak. Similarly, peaks at lower wavenumbers (1544.31, and 1366.57 cm^{-1}) also became prominent as compared with the ones observed in the unreacted clay. A small peak at 1720.34 cm^{-1} corresponding to O-H bending vibrations was also noted as a result of reaction. We also computed similar peaks that followed the same qualitative trends as shown in **Figure 2 (b)**.

Most importantly, we were able to capture the IR signatures of carbonate species with unprecedented levels of accuracy. In the deconvoluted IR spectra (**Figure S10**), we noted the emergence of a sharp peak at 1444.07 cm^{-1} that was associated with the bending vibration of C-O in carbonate ion (CO_3^{2-}) formed as a result of different carbonation reactions [54,55]. Simulated C-O bending peak for CO_3^{2-} was also observed at ~1450 cm^{-1} suggesting that the carbonate formation reactions may have been simulated accurately. Additionally, weak peaks ~3600-3800 cm^{-1} corresponding to the C-O stretching vibrations for CO_3^{2-} was observed in both experiments and simulations, further confirming the efficacy of the forcefield.

Figure S10 also shows peaks corresponding to various other expected reaction products. In case of the sample reacted with H_2O-HCOOH mixture, besides the peaks appearing at 1715.09, 1633.28, 1580.20, 1544.81, 1374.58 cm^{-1} for OH bending vibrations and 1442.84 cm^{-1} for C-O due to carbonation of NaOH, we also observed peaks around 1715.09 cm^{-1} (sharp), and 1664.73 cm^{-1}, which corresponded to the COO^- vibrations in HCOONa. A peak attributed to the vibrations of C=O groups was observed at 1685.83 cm^{-1}. Additionally, we also noted the vibrations from C-O group in carboxylic acid salts i.e., HCOONa in our case, at 1607.00 and 1392.96 cm^{-1} [56–59]. These peaks, however, are not quite apparent in the computed IR spectra, partly because the forcefield was not trained against these vibrational modes and partly because the concentration of these formed species was negligible to produce a characteristic signature.

3.2. Precipitation of solids at the interlayer

Reactions between the (bi)carbonate species and dissolved Na^+ cations result in the precipitation of Na_2CO_3 and $NaHCO_3$ solids that can potentially deposit at the interlayer[60]. As evident from the concentration profiles of the (bi)carbonate salts shown in **Figure S15** and **Figure S16**, the propensity to form $NaHCO_3$ and Na_2CO_3 is higher at the interlayer regime owing to the high concentration of Na^+ and H_2CO_3. The mechanism of $NaHCO_3$ and Na_2CO_3 precipitation as obtained from our MD simulations is shown in **Figure 3.** In this mechanism, dissolved Na^+ ion attacks the oxygen of H_2CO_3, followed by the formation of intermediate species, Na--H_2CO_3 (**Figure 3 (b))**, which dissociates to produce $NaHCO_3$ and proton, as shown in **Figure 3 (c).** To form Na_2CO_3, Na^+ ion attack the $NaHCO_3$ **Figure 3 (d)** releasing a proton via Na^+/H^+ exchange reaction **Figure 3 (e)**.

One direct consequence of this precipitation is the change in the interlayer basal spacing. To determine if salt precipitation alters the interlayer spacing, we inspect the peak positions in X-ray scattering measurements. The changes in the interlayer basal spacing of Na-montmorillonite as a result of reactions was determined using SAXS measurements. The combined USAXS and SAXS curves for samples in the study are shown in the **Figure 4**, wherein the zoomed-in SAXS portion is shown in **Figure 4 (b)**. Changes in the interlayer basal spacing of Na-montmorillonite were noted, depending on the reacting fluid. The interlayer basal spacing (*d*-spacing) for

unreacted clay was noted to be 12.36 Å. Upon reaction with H_2O, the interlayer spacing slightly increased to 14.01 Å. This value falls between the 1W and 2W hydration of Na-montmorillonite clays[17], which could be attributed to the precipitation of different species between the interlayers. Further, a slight hump after reaction with H_2O was also noted around q = 0.26 $Å^{-1}$, corresponding to the basal spacing of 24.17 Å ($d = 2\pi/q$). Peaks for the same interlayer spacing (24.17 Å) were also noted in case of reaction with HCOOH and 1:1 mixture of H_2O and HCOOH. This could be attributed to the precipitation of different species in the interlayer of swelling clays like Na-montmorillonite as reported previously[17,18,61]. Moreover, for both HCOOH and 1:1 mixture of H_2O and HCOOH, the original interlayer basal spacing of ~12 Å was also noted, which indicates that the original clay spacing has been largely preserved.

Other species with the potential to swell clays are NaOH and HCOONa. As shown in **Figure 7** and **Figure S13**, we observe an increasing concentration of NaOH and HCOONa molecules respectively, observed in MD simulations. In **Figure 5**, the WAXS intensities for Na-montmorillonite clay before and after reactions are shown. Some additional peaks were also noted in the WAXS pattern after reaction with the fluids. After reaction with H_2O, two prominent new peaks were noted around q = 2.99 and 3.48 $Å^{-1}$, corresponding to the interplanar d-spacing of 2.10 and 1.81 Å, respectively. These peaks correspond to the (200) and (220) planes of cubic NaOH [62], which was formed during the reaction.

Na-montmorillonite reacted with pure HCOOH and H_2O+HCOOH mixture resulted in the formation of Na_2CO_3 and HCOONa salts. These characteristic peaks noted at q = 1.67 and 1.81 $Å^{-1}$, in Na-montmorillonite (1:1, H_2O:HCOOH), correspond to ($\underline{1}11$) and (111) planes of monoclinic Na_2CO_3 [63] with the interplanar d-spacings of 3.74 and 3.44 Å, respectively. However, in case of acid (HCOOH) only, ($\underline{2}01$) and (111) planes of monoclinic NaOH were noted around 1.63 and 1.81 $Å^{-1}$, corresponding to the interplanar d-spacings of 3.86 and 3.48 Å, respectively. Moreover, additional peaks were also noted in both cases with formic acid. In 1:1 mixture, the peak around q = 3.93 $Å^{-1}$, having an interplanar d-spacing of 1.59 Å corresponds to the precipitation of HCOONa [64]. Na-montmorillonite reacted in HCOOH resulted in two peaks around 1.74 and 3.98 $Å^{-1}$ (and the corresponding interplanar d-spacings of 3.62 and 1.58 Å) which correspond to HCOONa [64]. These experimental

results confirm predictions from ReaxFF/MD simulations of the formation of carbonate and formate phases when Na-montmorillonite is reacted with HCOOH. In the following sections, we investigate the pathway of these reactions with the help of ReaxFF/MD simulation trajectory with emphasis on the differences in reactivity between Na-montmorillonite facets, edges, and interlayer regions.

3.3. Differences in the reactivities of facets, edges, and interlayers

Three distinct reactive surfaces can be identified on the Na-montmorillonite structure in **Figure 1**: facets, edges, and the interlayers. Edge surfaces are assumed to have the same stoichiometry and structure as the bulk crystal, with slight bond-length relaxation to account for over- or under-coordinated surface O atoms. [65] However, recent *ab initio* MD simulation results indicate that cations in the octahedral layer adopt a 5-fold coordination making it highly reactive. [66] Interlayers are like facets but consist of Na^+ counterions at the surface to balance the excess surface charge. They also have adsorbed water and formic acid near the surface that result in the formation of reactive surface hydroxyl groups. The presence of excess charge, adsorbed molecules, and surface hydroxyl groups make the edge and interlayers relatively more reactive than the facets. In this section, we explore the various reaction mechanisms stemming from these reactivity differences.

3.3.1. Physisorption properties of Na-montmorillonite surface

The first observed step in these mechanisms is the physisorption of the fluid molecules at the montmorillonite surfaces. **Figure S4** shows the early stage interactions (before 2.5 ps) at the interface of Na-montmorillonite-water/acid interfaces. These are non-reactive, physical adsorption events at time scales in the range of 0-2.5 ps, causing an increase in the density of adsorbed layer, setting stage for surface protonation events (see **Figures S4 (a)** and **(b))**. It is important to ensure that the forcefield accurately captures the adsorbed fluid layer at the montmorillonite surface. Physisorption is due to van der Waals and Coulombic forces between the dipoles of water and acid and the induced dipoles on the montmorillonite surface. Hence, a stable physiosorbed layer also confirms that the nonbonded interactions between the atoms of montmorillonite, water, and formic acid are

modeled accurately by the forcefield. We obtained an adsorbed layer with a thickness of ~1-2 Å as shown in **Figure S4**, which is comparable with prior MD calculations [16,67] and the energy of adsorption of ~1 kcal/mol, which is in line with the hydration energy reported elsewhere [68]. To confirm that the adsorption energy is predicted accurately for the right physical reasons, we characterized the adsorption behavior of the fluid molecules. On the Si-terminated surface, we found that most of the water is adsorbed by hydrogen bonding to bridging oxygen (BO) of the surface Si-O-Si linkage. In the case of formic acid, however, the hydrogen bound to C tends to bind with the bridging oxygen via hydrogen bonding. After complete physisorption, the reactions are turned on.

The change in concentration of the adsorbed water and formic acid species due to chemical reactions, as a function of time in the edge, interlayer, and facet regimes from t = 0 (fully physisorbed state) to t = 0.6 ns (end of simulation) for different fluid environments are shown in **Figure S6**. Note that these three regimes are defined by considering a cleavage plane at a perpendicular distance of 0.5 nm from the surfaces on either side. The edge and interlayer regions have adsorbed the highest concentration of fluid molecules, which may be ascribed to the presence of Na^+ ions resulting in a positively charged surface that attracts the oxygen groups. This is further corroborated by the fact that water being a polar molecule is in a more physisorbed state than formic acid.

3.3.2. Formation and utilization of hydroxyl groups

The dissociation of the adsorbed water or formic acid molecules over time and the associated decrease in the concentrations of these molecules over time is shown in **Figure 6**. The products of the dissociation of adsorbed water or formic acid molecules are protons (H^+) and hydroxyl (OH^-) ions. The OH- ions are produced from the decomposition of water at the surface by formation of silanol (Si-OH) groups as a result of surface protonation. [16] The ≡Si-O^- (NBO) sites on the silica/silicate surface react with the adsorbed water molecules to become protonated.[15,69,70] Compared with the silica/silicate surface, the exposed surfaces of Na-montmorillonite are the tetrahedral silicate layers with all the Si atoms being Q^4 species, meaning that Si of SiO_4 tetrahedron within the layer is connected by four bridging oxygens. OH^- ions are highly reactive and can result in several other crucial reactions that determine the final composition of the mixture. We also quantified the time dependent changes in

concentration of OH^- ions, as shown in **Figure 6**. As seen in the figure, for water + formic acid and pure formic acid cases, OH^- concentration increases to a peak value in 0.2 ns and then reduces (or stays nearly constant) with time for all three regions. However, for pure water case, OH^- concentration decreases as a result of interactions with the interlayer but increases due to interactions with the edge and facet regions. The decrease in OH^- concentrations is attributed to reactions with formic acid. Formic acid dissociates to release a proton that combines with OH^- to produce water leaving behind formate species following an acid-base neutralization reaction. These formate ions further react with OH^- to produce formaldehyde following the reaction: $HCOO^- + OH^- \rightarrow HCHO + O_2$. This results in an increased concentration of formaldehyde as shown in **Figure S7(b)**. In the pure water case, OH^- is mostly only consumed by Na^+ ions that are present in the interlayer, resulting in a steadily decreasing trend, as seen in **Figure S6**. OH^- ions are consumed by Na^+ ions as soon as they form, to produce NaOH molecules, which either deposit in the interlayer or diffuse outwards (**Figure S8**), thus contributing to the leaching of Na^+ ions.

It is important to note the gradually decreasing trend of OH^- concentrations in the interlayer region where Na-montmorillonite is reacted with formic acid compared with reactions with pure water at the edge and facet. This may be attributed to multiple competing reactions. In the interlayer region, OH^- concentration decreases because these ions are consumed by Na^+ ions as soon as they are produced, to form NaOH molecules (**Figure 7**). Moreover, the replenishment of OH^- ions by diffusion of water molecules to the interlayer is a comparatively slow process. For the edge and facet regions, however, continuous surface protonation constantly produces OH^- groups but the concentrations of NaOH at the edge and facet is substantially lower than that of the interlayer. Lower than expected consumption of OH^- ions is attributed to the slower diffusion of Na^+ ions compared to OH^- formation kinetics at the edges and the facets. This hypothesis is confirmed by the trends in HCOONa production rates as seen in **Figure S13**. The $HCOO^-$ molecules formed by the deprotonation of formic acid are neutralized with Na^+ ion to form sodium formate (**Figure S12**). Alternatively, these $HCOO^-$ molecules are adsorbed on the surface of Na-montmorillonite and converted to CO, CO_2, and carbonate (CO_3^{2-}) species based on the local conditions.

3.3.3. Conversion of HCOOH to CO, CO_2, and CO_3^{2-} groups

The interactions of formic acid and clays at elevated temperatures and pressures result in the formation of CO, CO_2, and CO_3^{2-} species. CO concentrations are particularly important since CO molecules are strong reducing agents, and the precursor to CO_2 formation which is eventually converted to bicarbonates and carbonates.

Figure 8 shows the concentration of CO in the different regimes as a function of time. For edge and interlayer, water + formic acid case yields higher CO concentration but for facets, pure HCOOH case results in a higher concentration. CO concentration increases with time in the interlayer but decreases in the facet region. In the edge region, in comparison, CO concentrations increase marginally up to 0.4 ns and then decrease. Interactions of formic acid and water mixtures with the edge and the interlayer result in higher levels of CO formation compared to formic acid. In contrast, formic acid produces more CO molecules due to interactions with the facet region of sodium montmorillonite. The mechanisms underlying these observations are discussed below.

There are two mechanisms involved in the formation of CO. In the first mechanism, CO is formed by the simple decomposition of HCOOH without any surface catalytic influences. In a surface catalyzed mechanism, the adsorbed water decomposes a formic acid molecule creating two water molecules and CO as shown in **Figure 9**. We performed independent bond restraint analysis on these two mechanisms, which yielded an activation energy barrier of ~59 kcal/mol for the surface catalyzed reaction and an activation energy of ~47 kcal/mol for the HCOOH decomposition reaction in the absence of a solid interface. Hence, these reactions have nearly equal probability of occurrence. For the case of simple decomposition, note that at 473 K, the kT energy ~1 kcal/mol is significantly lower than the energy barrier of ~47 kcal/mol. While the low kT energy may be insufficient to drive many such reactions in the system, for a single HCOOH molecule to decompose, it is only required that molecule absorbs enough vibrational energy for the C-O bond to vibrate, stretch, and eventually break. As temperature increases, we expect the concentration of CO to rise owing to higher kT energy. These reactions will be more prominent in the earth's subsurface where the temperatures could go up to several thousand kelvins. The same argument is also applicable to surface catalyzed HCOOH to CO conversion with an additional requirement of

water molecules and a catalytic surface, which are also likely be present in subsurface environments, making this alternate route equally significant. Nonetheless, in the bulk fluid, we expect more HCOOH decomposition reactions while in the presence of surfaces, we expect more surface catalyzed CO production reactions. For instance, the water + formic acid case has substantially more CO concentration for edge and interlayer regions because the high concentration of surface adsorbed water aids in CO production. At the facet, CO formation due to the decomposition of HCOOH is dominant.

The strong reducing nature of CO contributes to CO_2 formation. The 1:1 mixture of water and formic acid also produces more CO_2 molecules, in all cases, compared to the pure water or formic acid cases. In principle, HCOOH to CO_2 conversion can occur by three different mechanisms: direct, indirect, and the formate pathway, as represented by the reactions below:

1. $HCOOH \leftrightarrow HCOOH_{ad} \xrightarrow{-2H^+,-2e^-} CO_2$ (Direct pathway) (1)
2. $HCOOH \leftrightarrow HCOOH_{ad} \xrightarrow{-H^+,-e^-} HCOO^-_{ad} + ? \xrightarrow{-H^+,-e^-} CO_2$ (Formate pathway) (2)
3. $HCOOH \leftrightarrow HCOOH_{ad} \xrightarrow{-H_2O} CO_{ad} \xrightarrow{+H_2O,-2H^+,-2e^-} CO_2$ (Indirect pathway) (3)

Our simulations showed that the indirect mechanism as illustrated in **Figure 11** is the dominant source of CO_2. Here, the adsorbed CO molecules react with water at the surface to form CO_2. From the CO_2 concentration profile shown in **Figure 10**, it is clear that the CO molecules are consumed at the interlayer and produce more CO_2 molecules.

The concentration of CO_2 also begins reducing after 0.4 ns owing to the formation of carbonic acid. This manifests as the decrease in CO_2 concentration with time for edge and interlayer cases (**Figure 10**). Whereas for the facet, carbonic acid production is low and therefore, we observe a steady rise in CO_2 concentration. CO_2 molecules can further react with water and form carbonate species i.e. conversion of CO_2 to CO_3^{2-}. CO_3^{2-} concentration (**Figure 12**) changes only in the interlayer region whereas at edge and facet, it is non-existent. To interrogate the trends shown in **Figure 12** further, we analyzed the pathways of CO_3^{2-} formation, yielding two distinct mechanisms:

1. $CO_2 + H_2O \rightarrow H_2CO_3 \xrightarrow{-H^+} HCO_3^- \xrightarrow{-H^+} CO_3^{2-}$ (carbonic acid to carbonate decomposition as shown in **Figure S17** and **Figure S18**) (4)
2. $HCOO_{ad} + O^* \rightarrow CO_3^{2-} + H^+$ (surface catalyzed oxidation of adsorbed formate ion as shown in
3.
4. **Figure 13**). (5)

In the interlayer region, due to multiple clay sheets engulfing the formic acid molecules, both these reactions were observed in our simulations. To assess which reaction is more probable, we examined the H_2CO_3 concentration (**Figure 14**). For edges, although H_2CO_3 concentration is high, no carbonate molecules are formed but for interlayer, although the H_2CO_3 concentration is lower than the edges, carbonate concentration is higher. The trends shown in **Figure 12** and **Figure 14** can be explained by the combined effects of long residence time of adsorbed H_2CO_3 ions, presence of interlayer Na^+ and OH^- ions in the interlayer region. H_2CO_3 molecules formed at the facets and edges diffuse out into the bulk fluid whereas those adsorbed at the interlayer decomposes to CO_3^{2-} ions over time. The surrounding OH^- ions help in abstracting protons from H_2CO_3 and Na^+ ions in precipitating the carbonate salts. These effects are mutually complementing in the interlayer region whereas that is not observed at the edge and facet regions.

For the interlayer region, however, the number of carbonate ions produced from H_2CO_3 conversion and HCOO- conversion is in ~1:3 ratio. This suggests that the carbonate formation reaction from H_2CO_3 conversion has higher probability of occurrence. To confirm this hypothesis, we performed bond restraint analysis on both these reaction pathways. Decomposition of carbonic acid (as shown in **Figure 12**) and bicarbonate ions (as shown in **Figure 13**) was shown to have an activation energy of ~29 kcal/mol and ~34 kcal/mol, respectively. On the other hand, the activation of energy associated with the formation of CO_3^{2-} species from $HCOO^-$ adsorbed at the interlayer of Na-montmorillonite (as shown in **Figure 14**) was shown to have ~100 kcal/mol activation energy from bond restraint analysis. Therefore, it is energetically more favorable for carbonate production to proceed in the H_2CO_3 decomposition pathway, but the presence of mineral surfaces may invoke a surface catalyzed formate ion oxidation pathway, especially at high temperatures.

The formation of HCO_3^- and CO_3^{2-} ions (Equation 4) is the underlying cause of reprecipitation of $NaHCO_3$ and Na_2CO_3 described in Section 3.2. These precipitates can act as heterogeneous nucleation sites for further metal carbonate nuclei growth by different growth mechanisms observed by prior researchers like classical monomer-by-monomer addition and modern oriented attachment.[60,71,72]

3.3.4. Summary of speciation reactions

Considering the complexity in speciation behavior of clay surfaces, we have summarized the various interfacial and speciation reactions described in sections 3.3.2 and 3.3.3 in Table 1.

Table 1. Summary of interfacial and speciation reactions observed in ReaxFF/MD simulations

New species	**Reaction pathways**	**Observed activation/reaction sites**	**Energy barrier from bond restraint analysis (vacuum)**
OH^-	H_2O + --Si-O-Si-- → --Si-OH + ≡Si-O^-	Surface Si-O-Si linkages	70 kcal/mol[29]
HCHO	$HCOO^-$ + OH^- → HCHO + O_2	Bulk fluid	-
NaOH	Na^+ + OH^- → NaOH	Bulk fluid and hydroxylated surfaces	-
HCOONa	$HCOO^-$ + Na^+ → HCOONa	Adsorbed surfaces	-
CO	HCOOH → CO + H_2O	Bulk fluid	47 kcal/mol
	HCOOH + H_2O → CO + H_2O	Surfaces with adsorbed water and acid molecules	59 kcal/mol
CO_2	CO_{ad} +H_2O → $2H^+$ + CO_2	Surfaces with adsorbed CO	-
H_2CO_3	CO_2 + H_2O → H_2CO_3	Bulk fluid and surfaces	-
HCO_3^-	H_2CO_3 → HCO_3^- + H^+	Interlayer	29 kcal/mol
CO_3^{2-}	HCO_3^- → CO_3^{2-} + H^+	Interlayer	34 kcal/mol
	$HCOO_{ad}$ + O* → CO_3^{2-} + H^+ (O*: reactive dangling oxygen)	Interlayer adsorbed surfaces	100 kcal/mol
$NaHCO_3$	HCO_3^- + Na^+ → $NaHCO_3$	Interlayer	-
Na_2CO_3	$NaHCO_3$ + Na → Na_2CO_3 + H^+	Interlayer	-

The first column contains stable intermediate and final species produced during the reaction process. The second and third columns contain the corresponding reaction pathways and activation sites observed in our simulations. The last column gives the energy barriers for the key reactions corresponding to second column obtained from bond-restraint calculations performed in vacuum. Note that the energy barriers were only calculated for competing reactions to assess their relative significance. These results delineate the experimentally observed speciation behavior of Na-montmorillonite in aqueous and acidic media. These simulations advance the fundamental understanding of surface speciation behavior of clay minerals and can be employed to even more complicated systems of mixed clays and directly compared with experimental data.

4. Conclusions

In this study, we determined the speciation behavior when sodium montmorillonite is reacted in three different fluid environments (water, formic acid, and 1:1 water + formic acid) using ReaxFF/MD simulations, IR spectroscopy, and X-ray scattering (WAXS, SAXS) measurements. All the major peaks in the experimental IR spectra of Na-montmorillonite before and after reaction with water and formic acid, such as those corresponding to Si-O-Al linkages, O-H and CO_3^{2-} groups were predicted by ReaxFF/MD with reasonable levels of accuracy. Our MD simulations predict that bicarbonate (HCO_3^-) and carbonate (CO_3^{2-}) ions react with Na^+ to produce $NaHCO_3$ and Na_2CO_3 solid precipitates, respectively. A direct consequence of this precipitation – an increase in the interlayer spacing was observed as additional peaks in the SAXS intensity plot. Furthermore, WAXS intensities also showed strong signatures of NaOH and HCOONa which also have the tendency to precipitate in the interlayer regions. The differences in the reactivities of the edge, interlayer, and facet regions were noted from the simulations. The interlayer preferentially aided the formation of CO, CO_2, and carbonates over the edge and facet regions. The higher reactivity of the interlayer is attributed to the presence of Na^+ counterions owing to over/under-coordinated O-atoms and 5-fold coordination of cations in the octahedral layer. The facet region was the least reactive surface where most reactions were attributed to surface mediated decomposition of adsorbed species.

Molecular-level mechanistic insights of the speciation behavior of OH^- ions, CO, CO_2, and CO_3^{2-} were obtained from the MD simulations. In a pure water system, OH^- ions are consumed by Na^+ ions to form NaOH molecules that either deposit in the interlayer or leach outwards into water. In acid containing environments, OH^- ions are consumed by formic acid to produce water and formate ions, which further reduce to formaldehyde ($HCOO^- + OH^- \rightarrow HCHO + O_2$). Formation of CO due to simple decomposition of HCOOH and water-assisted surface catalytic decomposition of HCOOH was observed with both these pathways yielding energetically similar probability of occurrence. CO_2 formed by the indirect conversion of CO to CO_2 near the clay edge and interlayer surfaces. The formed CO_2 later converts to HCO_3^- and CO_3^{2-} molecules. The experimental and simulation approaches described in this study and the transferable forcefields for fluid-clay interactions can be applied translationally to advance the science of clay-fluid interactions for several applications including subsurface fluid storage and recovery and clay-pollutant dynamics.

Associated Content

The Supporting Information is available free of charge on the ACS Publications website.

Supplementary Information (PDF)

AUTHOR INFORMATION

Corresponding authors

Dr. Adri C. T. van Duin,

Phone: +1 814 863 6277, E-mail: acv13@engr.psu.edu

Dr. Greeshma Gadikota,

Phone: +1 607-255-4796. E-mail: gg464@cornell.edu

Author Contributions

M.G.M. and S.H.H. developed the forcefield, performed MD simulations and analysis with assistance from A.C.T.v.D. providing guidance. N.D. contributed in the forcefield development. H.A. performed the measurements with assistance from G.G. providing guidance. M.G.M. and H.A. wrote the majority of the manuscript with guidance from A.C.T.v.D. and G.G. All authors contributed to the writing and review of the manuscript. A.C.T.v.D. supervised the overall effort.

Funding Sources

This work was supported as part of the Multi-Scale Fluid-Solid Interactions in Architected and Natural Materials (MUSE), an Energy Frontier Research Center funded by the U.S. Department of Energy, Office of Science, Basic Energy Sciences under Award # DE-SC0019285. S.H.H. acknowledges support from NSF DMR grant # 1609107.

References

(1) Montgomery, W.; Tuff, J.; Kohn, S. C.; Jones, R. L. Reactions between Organic Acids and Montmorillonite Clay under Earth-Forming Conditions. *Chem. Geol.* **2011**, *283* (3–4), 171–176. https://doi.org/10.1016/j.chemgeo.2010.12.023.

(2) Bass, M. N. Montmorillonite and Serpentine in Orgueil Meteorite. *Geochim. Cosmochim. Acta* **1971**, *35* (2), 139–147. https://doi.org/10.1016/0016-7037(71)90053-6.

(3) Tomeoka, K.; Buseck, P. R. Intergrown Mica and Montmorillonite in the Allende Carbonaceous Chondrite. *Nature* **1982**, *299* (5881), 326–327. https://doi.org/10.1038/299326a0.

(4) Sephton, M. A. Organic Compounds in Carbonaceous Meteorites. *Nat. Prod. Rep.* **2002**, *19* (3), 292–311. https://doi.org/10.1039/b103775g.

(5) Ferris, J. P.; Delano, J. W. Chemical Evolution Across Space and Time; American Chemical Society, 2017; pp 292–308.

(6) Ehrenfreund, P.; Charnley, S. B. Organic Molecules in the Interstellar Medium, Comets and Meteorites: A Voyage from Dark Clouds to the Early Earth. *Rev. Astron. Astrophys.* **2000**, *38*, 427–483.

(7) Gadikota, G.; Zhang, F.; Allen, A. J. Towards Understanding the Microstructural and Structural Changes in Natural Hierarchical Materials for Energy Recovery: In-Operando Multi-Scale X-Ray Scattering Characterization of Na- and Ca-Montmorillonite on Heating to 1150 °C. *Fuel* **2017**, *196*, 195–209. https://doi.org/10.1016/j.fuel.2017.01.092.

(8) Kaszuba, J. P.; Janecky, D. R.; Snow, M. G. Carbon Dioxide Reaction Processes in a Model Brine Aquifer at 200 C and 200 Bars: Implications for Geologic Sequestration of Carbon. *Appl. Geochemistry* **2003**, *18* (7), 1065–1080.

(9) Herz-Thyhsen, R. J.; Kaszuba, J. P.; Dewey, J. C. Dissolution of Minerals and Precipitation of an Aluminosilicate Phase during Experimentally Simulated Hydraulic Fracturing of a Mudstone and a Tight Sandstone in the Powder River Basin, WY. *Energy & Fuels* **2019**, *33*, 3947–3956.

(10) Li, M.; Wei, C.; Fan, G.; Li, C.; Deng, Z.; Li, X. Extraction of Vanadium from Black Shale Using Pressure Acid Leaching. *Hydrometallurgy* **2009**, *98* (3–4), 308–313.

(11) El Rayah, H. M. E.; Rowell, D. L. The Influence of Iron and Aluminium Hydroxides on the Swelling of Na-Montmorillonite and the Permeability of Na-Soil. *J. Soil Sci.* **1973**, *24* (1), 137–144. https://doi.org/10.1111/j.1365-2389.1973.tb00749.x.

(12) Brindley, G. W.; Kao, C.-C. Formation, Compositions, and Properties of Hydroxy-Al- and Hydroxy-Mg-Montmorillonite. *Clays Clay Miner.* **1980**, *28* (6), 435–443.

(13) Lagaly, G.; Mecking, O.; Penner, D. Colloidal Magnesium Aluminum Hydroxide and Heterocoagulation with a Clay Mineral. II. Heterocoagulation with Sodium Montmorillonite. *Colloid Polym. Sci.* **2001**, *279* (11), 1097–1103. https://doi.org/10.1007/s003960100525.

(14) Smith, M. M.; Dai, Z.; Carroll, S. A. Illite Dissolution Kinetics from 100 to 280° C and PH 3 to 9. *Geochim. Cosmochim. Acta* **2017**, *209*, 9–23.

(15) Hahn, S. H.; van Duin, A. C. T. Surface Reactivity and Leaching of a Sodium Silicate Glass Under Aqueous Environment: A ReaxFF Molecular Dynamics Study. *J. Phys. Chem. C* **2019**.

(16) Muraleedharan, M. G.; Herz-Thyhsen, R.; Dewey, J. C.; Kaszuba, J.; van Duin, A. C. T. Understanding

the Chemistry of Cation Leaching in Illite/Water Interfacial System Using Reactive Molecular Dynamics Simulations and Hydrothermal Experiments. *Acta Mater.* **2020**, *186*, 564–574.

(17) Hur, T. B.; Baltrus, J. P.; Howard, B. H.; Harbert, W. P.; Romanov, V. N. Carbonate Formation in Wyoming Montmorillonite under High Pressure Carbon Dioxide. *Int. J. Greenh. Gas Control* **2013**, *13*, 149–155. https://doi.org/10.1016/j.ijggc.2012.12.001.

(18) Giesting, P.; Guggenheim, S.; Koster van Groos, A. F.; Busch, A. Interaction of Carbon Dioxide with Na-Exchanged Montmorillonite at Pressures to 640 Bars: Implications for CO2 Sequestration. *Int. J. Greenh. Gas Control* **2012**, *8*, 73–81. https://doi.org/10.1016/j.ijggc.2012.01.011.

(19) Ferrage, E.; Sakharov, B. A.; Michot, L. J.; Delville, A.; Bauer, A.; Lanson, B.; Grangeon, S.; Frapper, G.; Jiménez-Ruiz, M.; Cuello, G. J. Hydration Properties and Interlayer Organization of Water and Ions in Synthetic Na-Smectite with Tetrahedral Layer Charge. Part 2. Toward a Precise Coupling between Molecular Simulations and Diffraction Data. *J. Phys. Chem. C* **2011**, *115* (5), 1867–1881.

(20) Botan, A.; Rotenberg, B.; Marry, V.; Turq, P.; Noetinger, B. Carbon Dioxide in Montmorillonite Clay Hydrates: Thermodynamics, Structure, and Transport from Molecular Simulation. *J. Phys. Chem. C* **2010**, *114* (35), 14962–14969.

(21) Yu, Y.; Yang, X. Molecular Simulation of Swelling and Interlayer Structure for Organoclay in Supercritical CO 2. *Phys. Chem. Chem. Phys.* **2011**, *13* (1), 282–290.

(22) Suter, J. L.; Coveney, P. V; Greenwell, H. C.; Thyveetil, M.-A. Large-Scale Molecular Dynamics Study of Montmorillonite Clay: Emergence of Undulatory Fluctuations and Determination of Material Properties. *J. Phys. Chem. C* **2007**, *111* (23), 8248–8259.

(23) Mazo, M. A.; Manevitch, L. I.; Gusarova, E. B.; Shamaev, M. Y.; Berlin, A. A.; Balabaev, N. K.; Rutledge, G. C. Molecular Dynamics Simulation of Thermomechanical Properties of Montmorillonite Crystal. 1. Isolated Clay Nanoplate. *J. Phys. Chem. B* **2008**, *112* (10), 2964–2969.

(24) Aristilde, L.; Marichal, C.; Miehe-Brendle, J.; Lanson, B.; Charlet, L. Interactions of Oxytetracycline with a Smectite Clay: A Spectroscopic Study with Molecular Simulations. *Environ. Sci. Technol.* **2010**,

44 (20), 7839–7845.

(25) Voora, V. K.; Al-Saidi, W. A.; Jordan, K. D. Density Functional Theory Study of Pyrophyllite and M-Montmorillonites (M= Li, Na, K, Mg, and Ca): Role of Dispersion Interactions. *J. Phys. Chem. A* **2011**, *115* (34), 9695–9703.

(26) Larentzos, J. P.; Greathouse, J. A.; Cygan, R. T. An Ab Initio and Classical Molecular Dynamics Investigation of the Structural and Vibrational Properties of Talc and Pyrophyllite. *J. Phys. Chem. C* **2007**, *111* (34), 12752–12759.

(27) Van Duin, A. C. T.; Dasgupta, S.; Lorant, F.; Goddard, W. A. ReaxFF: A Reactive Force Field for Hydrocarbons. *J. Phys. Chem. A* **2001**, *105* (41), 9396–9409.

(28) Chenoweth, K.; Van Duin, A. C. T.; Goddard, W. A. ReaxFF Reactive Force Field for Molecular Dynamics Simulations of Hydrocarbon Oxidation. *J. Phys. Chem. A* **2008**, *112* (5), 1040–1053.

(29) Muraleedharan, M. G.; Asgar, H.; Mohammed, S.; Gadikota, G.; van Duin, A. C. T. Elucidating Thermally Induced Structural and Chemical Transformations in Kaolinite Using Reactive Molecular Dynamics Simulations and X-Ray Scattering Measurements. *Chem. Mater.* **2019**.

(30) Pitman, M. C.; Van Duin, A. C. T. Dynamics of Confined Reactive Water in Smectite Clay–Zeolite Composites. *J. Am. Chem. Soc.* **2012**, *134* (6), 3042–3053.

(31) Bonse, U.; Hart, M. Tailless X-Ray Single-Crystal Reflection Curves Obtained by Multiple Reflection. *Appl. Phys. Lett.* **1965**, *7* (9), 238–240. https://doi.org/10.1063/1.1754396.

(32) Ilavsky, J.; Zhang, F.; Allen, A. J.; Levine, L. E.; Jemian, P. R.; Long, G. G. Ultra-Small-Angle X-Ray Scattering Instrument at the Advanced Photon Source: History, Recent Development, and Current Status. *Metall. Mater. Trans. A Phys. Metall. Mater. Sci.* **2013**, *44* (1), 68–76. https://doi.org/10.1007/s11661-012-1431-y.

(33) Nyam-Osor, M.; Soloviov, D. V.; Kovalev, Y. S.; Zhigunov, A.; Rogachev, A. V.; Ivankov, O. I.; Erhan, R. V.; Kuklin, A. I. Silver Behenate and Silver Stearate Powders for Calibration of SAS Instruments. *J. Phys. Conf. Ser.* **2012**, *351*, 012024. https://doi.org/10.1088/1742-6596/351/1/012024.

(34) Ilavsky, J.; Jemian, P. R. Irena: Tool Suite for Modeling and Analysis of Small-Angle Scattering. *J. Appl. Crystallogr.* **2009**, *42*, 347–353.

(35) Ilavsky, J. Nika: Software for Two- Dimensional Data Reduction. *J. Appl. Crystallogr.* **2012**, *45* (2), 324–326.

(36) Mortier, W. J.; Ghosh, S. K.; Shankar, S. Electronegativity-Equalization Method for the Calculation of Atomic Charges in Molecules. *J. Am. Chem. Soc.* **1986**, *108* (15), 4315–4320.

(37) Senftle, T. P.; Hong, S.; Islam, M. M.; Kylasa, S. B.; Zheng, Y.; Shin, Y. K.; Junkermeier, C.; Engel-Herbert, R.; Janik, M. J.; Aktulga, H. M.; et al. The ReaxFF Reactive Force-Field: Development, Applications and Future Directions. *npj Comput. Mater.* **2016**, *2* (September 2015). https://doi.org/10.1038/npjcompumats.2015.11.

(38) Hahn, S. H.; Rimsza, J.; Criscenti, L.; Sun, W.; Deng, L.; Du, J.; Liang, T.; Sinnott, S. B.; Van Duin, A. C. T. Development of a ReaxFF Reactive Force Field for NaSiO x/Water Systems and Its Application to Sodium and Proton Self-Diffusion. *J. Phys. Chem. C* **2018**, *122* (34), 19613–19624.

(39) Hantal, G.; Brochard, L.; Laubie, H.; Ebrahimi, D.; Pellenq, R. J.-M.; Ulm, F.-J.; Coasne, B. Atomic-Scale Modelling of Elastic and Failure Properties of Clays. *Mol. Phys.* **2014**, *112* (9–10), 1294–1305.

(40) Sadat, M. R.; Muralidharan, K.; Zhang, L. Reactive Molecular Dynamics Simulation of the Mechanical Behavior of Sodium Aluminosilicate Geopolymer and Calcium Silicate Hydrate Composites. *Comput. Mater. Sci.* **2018**, *150*, 500–509.

(41) Yu, Y.; Krishnan, N. M. A.; Smedskjaer, M. M.; Sant, G.; Bauchy, M. The Hydrophilic-to-Hydrophobic Transition in Glassy Silica Is Driven by the Atomic Topology of Its Surface. *J. Chem. Phys.* **2018**, *148* (7), 74503.

(42) DeAngelis, F.; Muraleedharan, M. G.; Moon, J.; Seyf, H. R.; Minnich, A. J.; McGaughey, A. J. H.; Henry, A. Thermal Transport in Disordered Materials. *Nanoscale Microscale Thermophys. Eng.* **2019**, *23* (2), 81–116. https://doi.org/10.1080/15567265.2018.1519004.

(43) Muraleedharan, M. G.; Van Duin, A. Reactive Molecular Dynamics Approach to Understand the

Chemistry-Driven Structural Transformations in Heat-Treated Clay Minerals. In *Abstracts Of Papers Of The American Chemical Society*; Amer Chemical Soc 1155 16th St, Nw, Washington, Dc 20036 Usa, 2019; Vol. 258.

(44) Dasgupta, N.; Shin, Y. K.; Fedkin, M. V; van Duin, A. ReaxFF Molecular Dynamics Simulations of Electrolyte–Water Systems at Supercritical Temperature. *J. Chem. Phys.* **2020**, *152* (20), 204502.

(45) Dasgupta, N.; Shin, Y. K.; Fedkin, M. V; van Duin, A. C. T. ReaxFF Molecular Dynamics Simulations on the Structure and Dynamics of Electrolyte Water Systems at Ambient Temperature. *Comput. Mater. Sci.* **2020**, *172*, 109349.

(46) Baerends, E. J.; Ziegler, T.; Atkins, A. J.; Autschbach, J.; Bashford, D.; Baseggio, O.; Bérces, A.; Bickelhaupt, F. M.; Bo, C.; Boerritger, P. M.; et al. ADF2019.3, SCM, Theoretical Chemistry, Vrije Universiteit, Amsterdam, The Netherlands, Https://Www.Scm.Com.

(47) Allen, M. P.; Tildesley, D. J. *Computer Simulation of Liquids*; Oxford university press, 2017.

(48) Plimpton, S. *Fast Parallel Algorithms for Short-Range Molecular Dynamics*; Sandia National Labs., Albuquerque, NM (United States), 1993.

(49) Plimpton, S.; Crozier, P.; Thompson, A. LAMMPS-Large-Scale Atomic/Molecular Massively Parallel Simulator. *Sandia Natl. Lab.* **2007**, *18*, 43.

(50) Bornhauser, P.; Bougeard, D. Intensities of the Vibrational Spectra of Siliceous Zeolites by Molecular Dynamics Calculations. I. Infrared Spectra. *J. Phys. Chem. B* **2001**, *105* (1), 36–41.

(51) Tireli, A. A.; Guimarães, I. do R.; Terra, J. C. de S.; da Silva, R. R.; Guerreiro, M. C. Fenton-like Processes and Adsorption Using Iron Oxide-Pillared Clay with Magnetic Properties for Organic Compound Mitigation. *Environ. Sci. Pollut. Res.* **2014**, *22* (2), 870–881. https://doi.org/10.1007/s11356-014-2973-x.

(52) Schuttlefield, J. D.; Cox, D.; Grassian, V. H. An Investigation of Water Uptake on Clays Minerals Using ATR-FTIR Spectroscopy Coupled with Quartz Crystal Microbalance Measurements. *J. Geophys. Res. Atmos.* **2007**, *112* (21), 1–14. https://doi.org/10.1029/2007JD008973.

(53) Malhotra, V. M.; Ogloza, A. A. FTIR Spectra of Hydroxyls and Dehydroxylation Kinetics Mechanism in Montmorillonite. *Phys. Chem. Miner.* **1989**, *16* (4), 386–393. https://doi.org/10.1007/BF00199560.

(54) Jin, F. Q.; Yang, R.; Zhang, J. C.; Li, M.; Hao, X. M.; Zhang, H. The State of NaOH in NaOH/Poly(Sodium Acrylate) Composite. *J. Dispers. Sci. Technol.* **2009**, *30* (8), 1148–1151. https://doi.org/10.1080/01932690802701614.

(55) Using, M.; Transform, F.; Spectroscopy, I.; Joshi, S.; Kalyanasundaram, S.; Balasubramanian, V. Quantitative Analysis of Sodium Carbonate and Sodium Bicarbonate in Solid Quantitative Analysis of Sodium Carbonate and Sodium Bicarbonate in Solid Mixtures Using Fourier Transform Infrared Spectroscopy (FT-IR). **2013**, No. January 2018, 1–6. https://doi.org/10.1366/12-06915.

(56) Newman, R. Polarized Infrared Spectrum of Sodium Nitrite. *J. Chem. Phys.* **1952**, *20* (3), 444–446. https://doi.org/10.1063/1.1700439.

(57) Maas, J. P. M. The Far Infrared Absorption Spectrum and the Assignment of the Lattice Modes of Sodium Formate. *Spectrochim. Acta Part A Mol. Spectrosc.* **1977**, *33* (8), 761–765. https://doi.org/10.1016/0584-8539(77)80114-1.

(58) Spinner, E.; Rowe, J. E. The Effects of Isotopic Dilution on the Infrared Spectrum of Solid Sodium Formate. *Aust. J. Chem.* **1979**, *32* (3), 481–501. https://doi.org/10.1071/CH9790481.

(59) Mate, B.; Herrero, V. J.; Escribano, R. Formate Ion : Structure and Spectroscopic Properties. **2011**, 70–75.

(60) Ruiz-Agudo, E.; Putnis, C. V; Putnis, A. Coupled Dissolution and Precipitation at Mineral–Fluid Interfaces. *Chem. Geol.* **2014**, *383*, 132–146.

(61) Yang, W.; Zaoui, A. Capture and Sequestration of CO2 in the Interlayer Space of Hydrated Calcium Montmorillonite Clay under Various Geological Burial Depth. *Phys. A Stat. Mech. its Appl.* **2016**, *449* (xxxx), 416–425. https://doi.org/10.1016/j.physa.2015.12.032.

(62) Natl. Bur. Stand. (U.S.) Managr. **1966**, *25* (4), 69.

(63) Technisch Physische Dienst. ICDD Grant-in-Aid: Delft, Netherlands 1967.

(64) Kang, L.; Li, S.; Wang, B.; Li, X. The Effect of High Pressure on the Structure and Stability of Sodium Formate: Probed by in Situ Synchrotron X-Ray Diffraction Technique. *Solid State Commun.* **2019**, *289* (October 2018), 67–70. https://doi.org/10.1016/j.ssc.2018.12.009.

(65) Liu, X.; Lu, X.; Meijer, E. J.; Wang, R.; Zhou, H. Atomic-Scale Structures of Interfaces between Phyllosilicate Edges and Water. *Geochim. Cosmochim. Acta* **2012**, *81*, 56–68.

(66) Bickmore, B. R.; Rosso, K. M.; Nagy, K. L.; Cygan, R. T.; Tadanier, C. J. Ab Initio Determination of Edge Surface Structures for Dioctahedral 2: 1 Phyllosilicates: Implications for Acid-Base Reactivity. *Clays Clay Miner.* **2003**, *51* (4), 359–371.

(67) Muraleedharan, M. G.; Sundaram, D. S.; Henry, A.; Yang, V. Thermal Conductivity Calculation of Nano-Suspensions Using Green-Kubo Relations with Reduced Artificial Correlations. *J. Phys. Condens. Matter* **2017**, *29* (15). https://doi.org/10.1088/1361-648X/aa5f08.

(68) Van Olphen, H. Thermodynamics of Interlayer Adsorption of Water in Clays. I.—Sodium Vermiculite. *J. Colloid Sci.* **1965**, *20* (8), 822–837.

(69) Mahadevan, T. S.; Du, J. Evaluating Water Reactivity at Silica Surfaces Using Reactive Potentials. *J. Phys. Chem. C* **2018**, *122* (18), 9875–9885.

(70) Fogarty, J. C.; Aktulga, H. M.; Grama, A. Y.; Van Duin, A. C. T.; Pandit, S. A. A Reactive Molecular Dynamics Simulation of the Silica-Water Interface. *J. Chem. Phys.* **2010**, *132* (17), 174704.

(71) De Yoreo, J.; Mandrus, D.; Soderholm, L. *Basic Research Needs for Synthesis Science*; 2016.

(72) Putnis, A. Why Mineral Interfaces Matter. *Science (80-.).* **2014**, *343* (6178), 1441–1442.

List of Figures

Figure 12. CO_3^{2-} concentrations as a function of reaction time at the edge, interlayer, and facet of Na-montmorillonite in 1:1 mixture of water and formic acid and formic acid are shown. (Zero error bar indicates that all three simulation runs yielded same concentrations).

Figure 13. Mechanisms involved in the formation of CO_3^{2-} species from $HCOO^-$ adsorbed at the interlayer of Na-montmorillonite by binding to the Al or Si site where **(a)** represents the simultanous attack of one dangling O of montmorillonite on C of $HCOO^-$ and weakening of C=O double bond followed by the formation of -C-O-Al/Si bridge as shown in **(b)**, and the formation of CO_3^{2-} which remains in adsorbed state and is neutralized by protons or Na^+ ions as represented by **(c)**.

Figure 14. Carbonic acid (H_2CO_3) concentration as a function of reaction time at the (a) edge, (a) interlayer, and (c) facet of Na-montmorillonite in 1:1 mixture of water and formic acid.

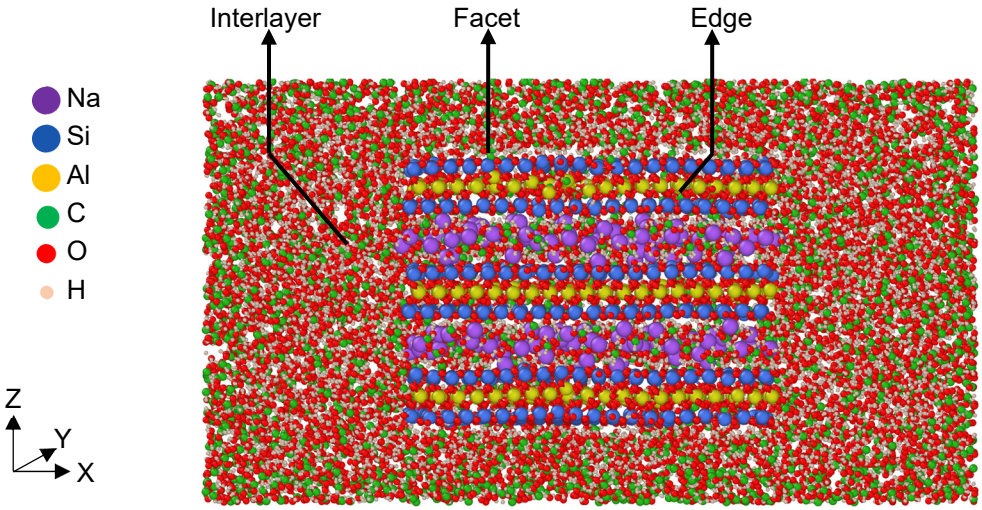

Figure 1. Snapshot of the simulated initial configuration of the molecular simulation showing Na-montmorillonite, water and formic acid molecules at 473 K and 1 bar.

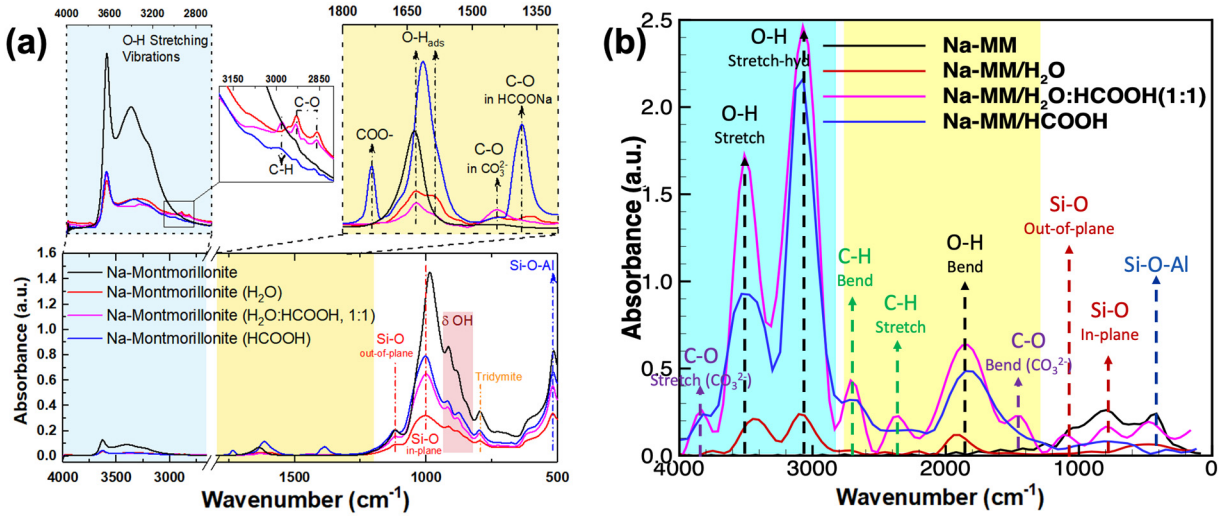

Figure 2. Comparison of (a) experimental and (b) computed IR spectra for unreacted Na-montmorillonite (Na-MM), Na-MM reacted in water, water and formic acid ratio of 1:1, and in formic acid with a purity of 98-100% at 200 °C and 1 atm for a reaction time of 2 hours.

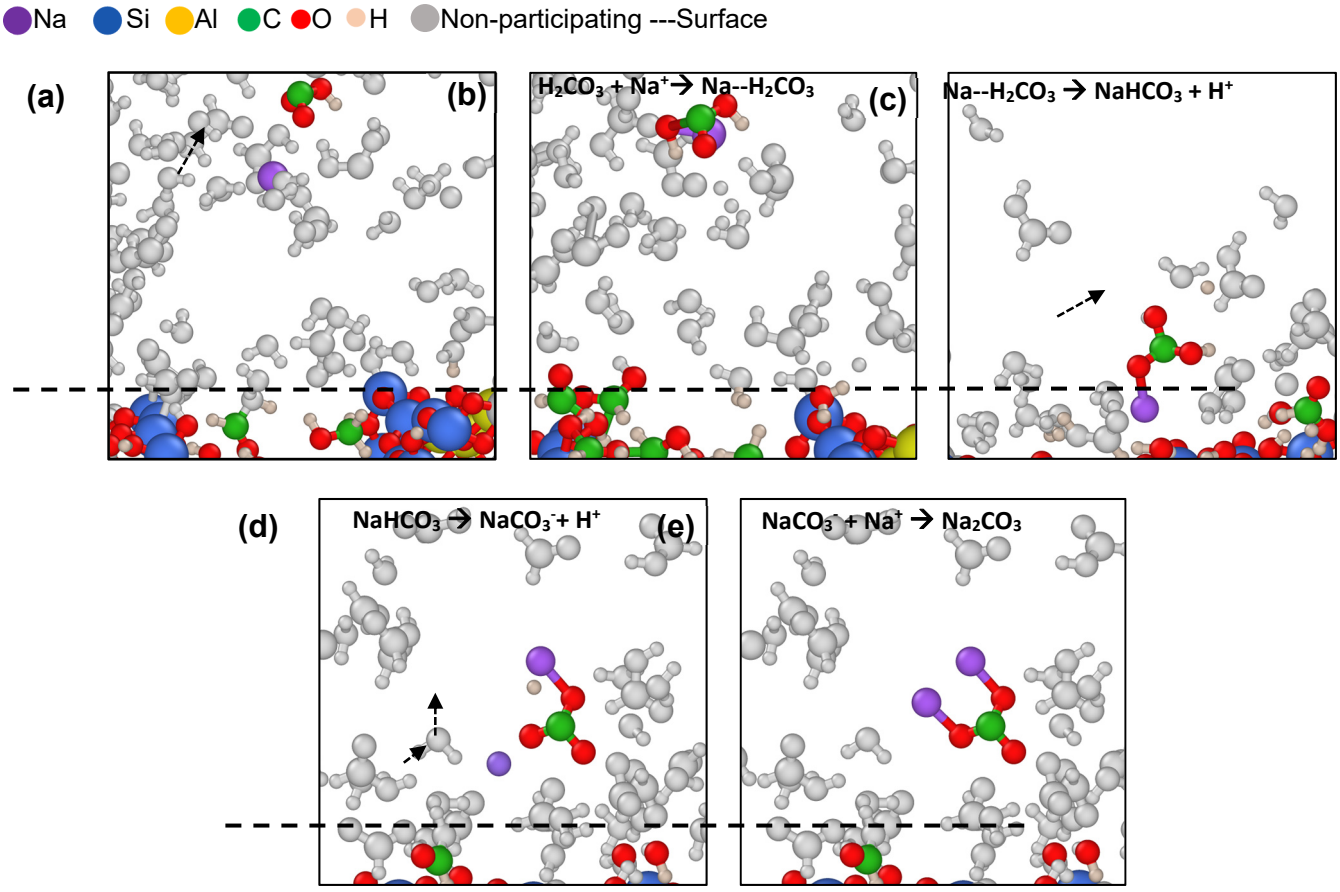

Figure 3. Mechanisms involved in the formation of sodium bicarbonate ($NaHCO_3$) near the interlayer of Na-montmorillonite where **(a)** represents the interactions between Na^+ ion and the oxygen of H_2CO_3, followed by the formation of intermediate species, Na--H_2CO_3 as shown in **(b)**. This intermediate species dissociates to produce $NaHCO_3$ and proton, as shown in **(c)**. **(d)** Na^+ ion attacks the oxygen of OH group of $NaHCO_3$ resulting in **(e)** Na_2CO_3 formation.

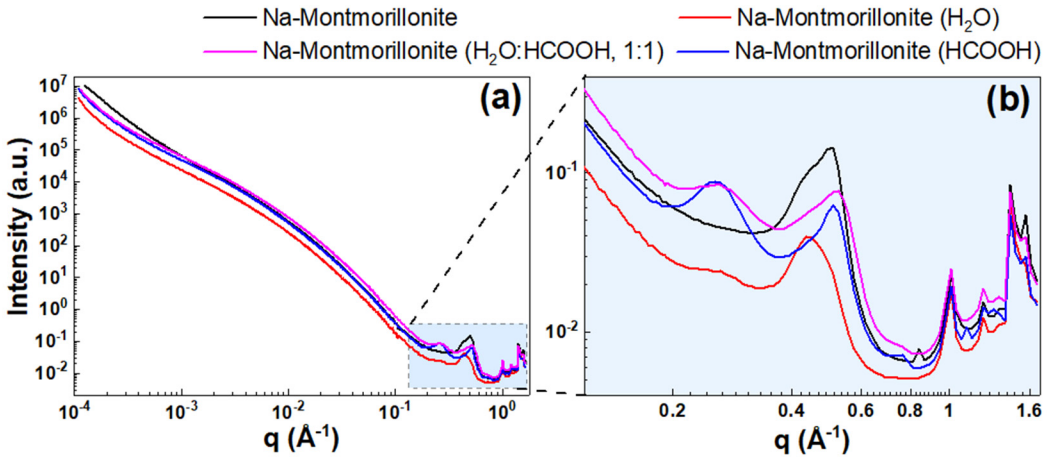

Figure 4. Changes in the interlayer basal spacing of Na-montmorillonite after reacting with water, HCOOH, and, 1:1 mixture of HCOOH and water at 200 °C and 1 atm for 2 hours using Ultra-Small Angle Scattering/Small Angle X-Ray Scattering (USAXS/SAXS) measurements.

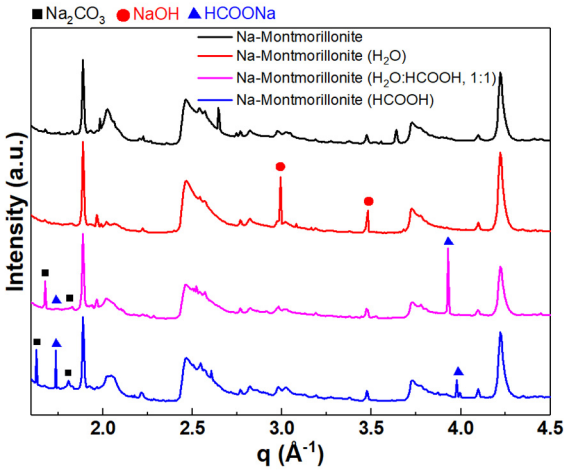

Figure 5. Evidence of the formation of Na_2CO_3, NaOH, and HCOONa due to reaction of Na-montmorillonite with water, 1:1 mixture of water and formic acid, and formic acid (98-100%)) at 200 °C and 1 atm for a reaction time of 2 hours using Wide Angle X-Ray Scattering (WAXS) measurements.

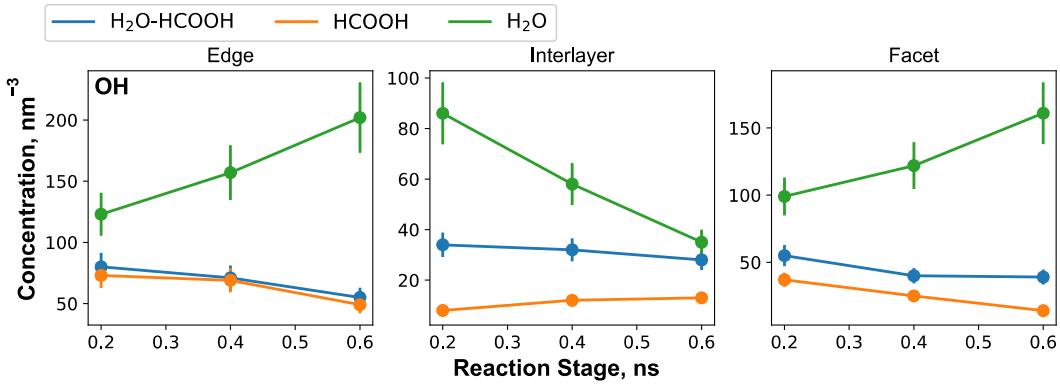

Figure 6. The concentration of hydroxyl ions as a function of time at the edge, interlayer and facet of Na-montmorillonite for various fluidic environments such as a 1:1 mixture of water and formic acid, formic acid, and water.

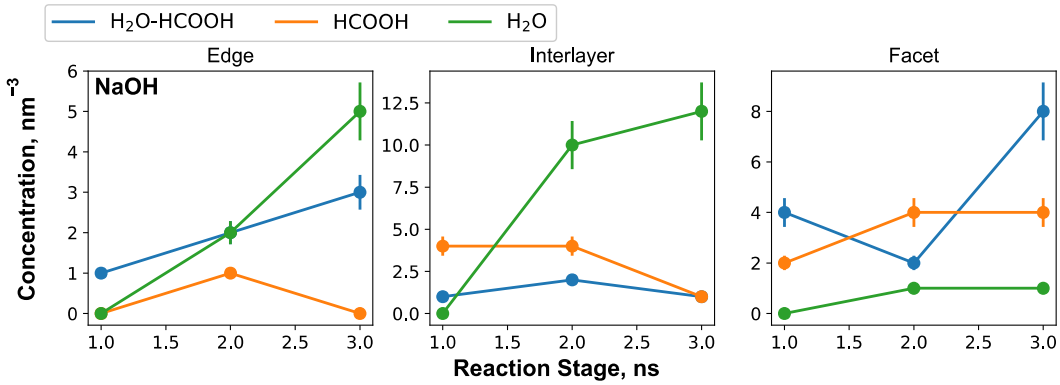

Figure 7. NaOH concentrations as a function of reaction time at the edge, interlayer, and facets of Na-montmorillonite in various fluidic environments such as a 1:1 mixture of water and formic acid, formic acid, and water.

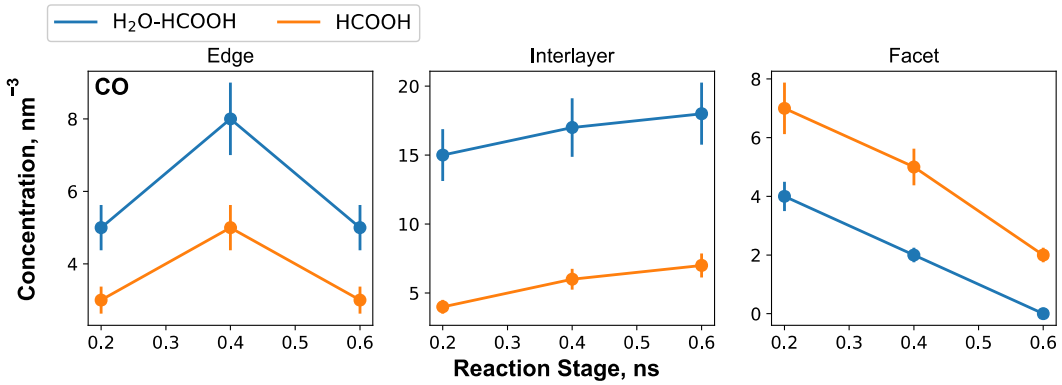

Figure 8. CO concentrations as a function of reaction time at the edge, interlayer, and facet of Na-montmorillonite in 1:1 mixture of water and formic acid and formic acid are shown.

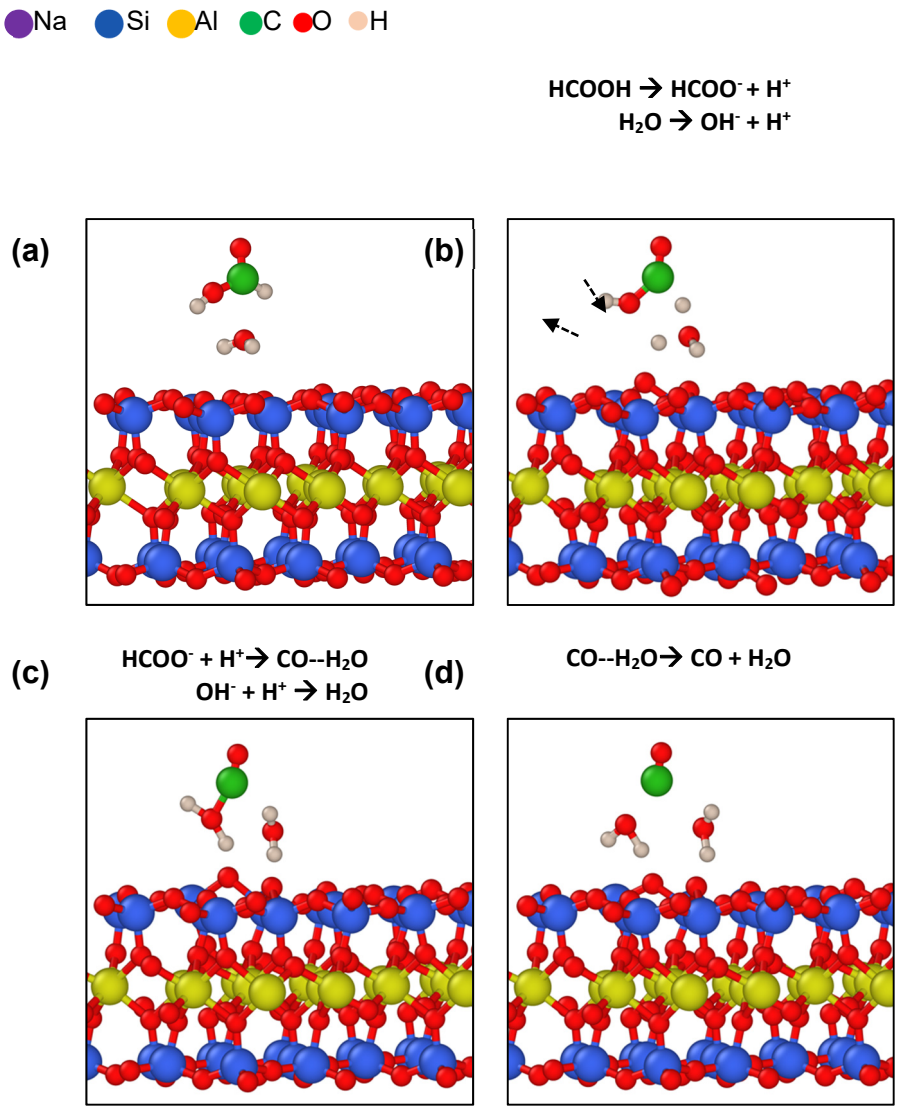

Figure 9. Mechanisms involved in CO formation due to surface water catalysis where **(a)** represents the interactions between the water adsorbed on the surface and the formic acid molecule, **(b)** represents proton abstraction from C-H bond of formic acid to water and from water to oxygen resulting from hydrogen bonding

(c) represents the formation of intermediate species: CO-H_2O, and **(d)** shows the formation of CO and H_2O molecules.

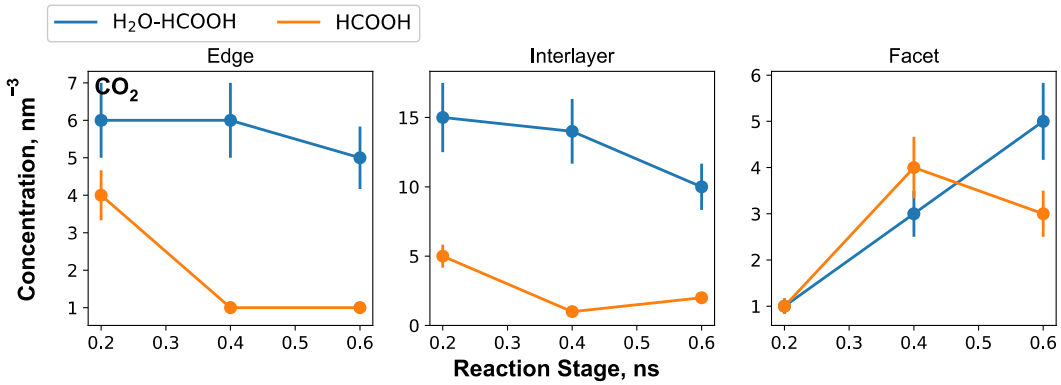

Figure 10. CO_2 concentrations as a function of reaction time at the (a) edge, (a) interlayer, and (c) facet of Na-montmorillonite in 1:1 mixture of water and formic acid and formic acid are shown.

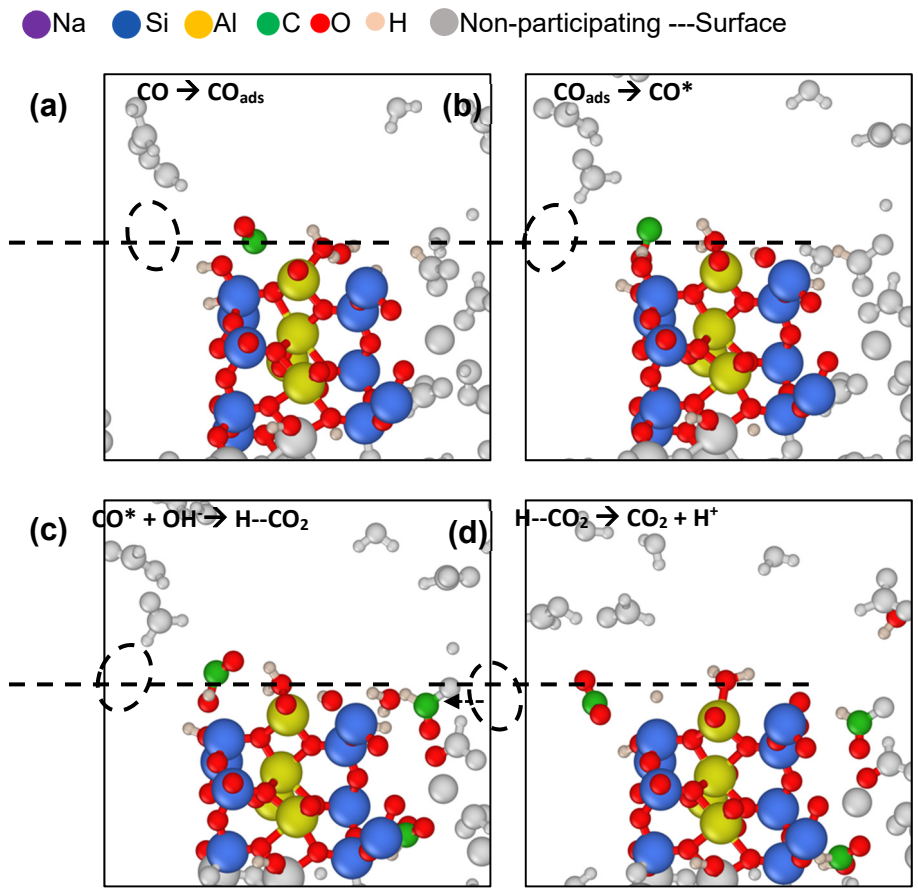

Figure 11. Mechanisms of CO_2 formation resulting from the oxidation of CO catalyzed at Na-montmorillonite surfaces where **(a)** shows the adsorption of CO on the surface site, **(b)** represents the formation of intermediate species CO*, **(c)** represents the formation of intermediate species, H--CO_2, and **(d)** represents the formation of CO_2 and a proton.

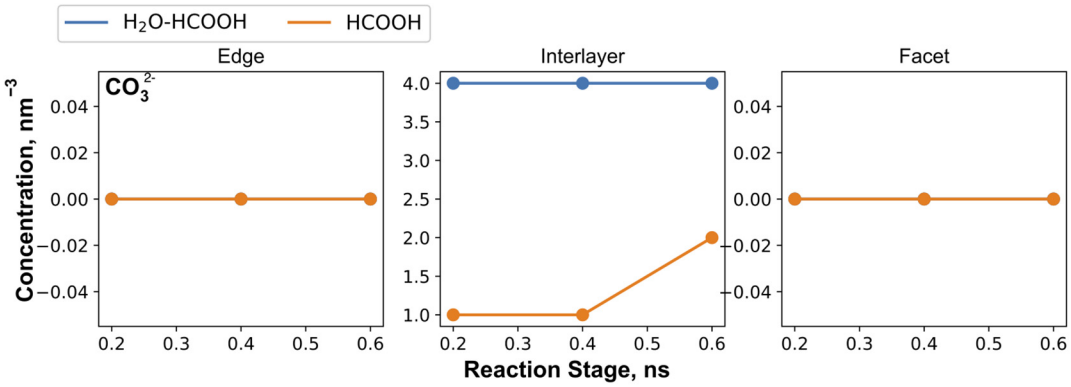

Figure 12. CO_3^{2-} concentrations as a function of reaction time at the edge, interlayer, and facet of Na-montmorillonite in 1:1 mixture of water and formic acid and formic acid are shown. (Zero error bar indicates that all three simulation runs yielded same concentrations).

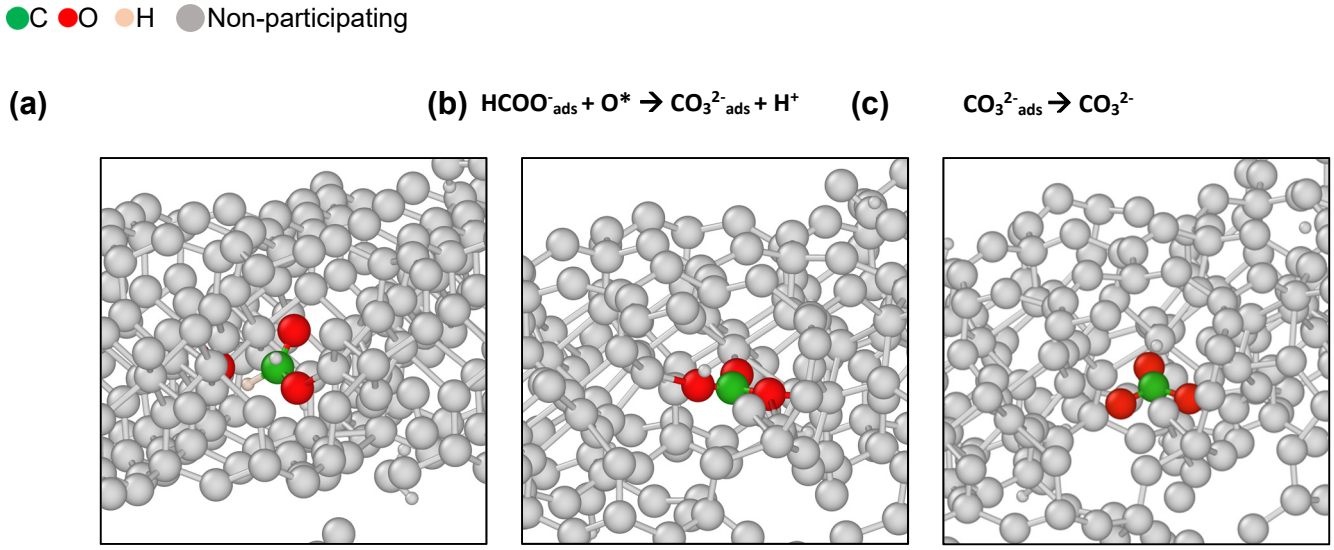

Figure 13. Mechanisms involved in the formation of CO_3^{2-} species from $HCOO^-$ adsorbed at the interlayer of Na-montmorillonite by binding to the Al or Si site where **(a)** represents the simultanous attack of one dangling O of montmorillonite on C of $HCOO^-$ and weakening of C=O double bond followed by the formation of -C-O-Al/Si bridge as shown in **(b)**, and the formation of CO_3^{2-} which remains in adsorbed state and is neutralized by protons or Na^+ ions as represented by **(c)**.

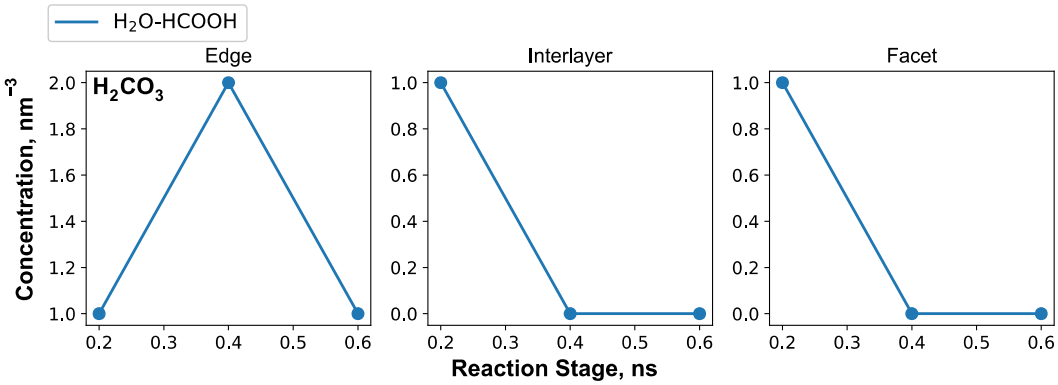

Figure 14. Carbonic acid (H_2CO_3) concentration as a function of reaction time at the (a) edge, (a) interlayer, and (c) facet of Na-montmorillonite in 1:1 mixture of water and formic acid.

TOC graphics